Ruocco *et al.*
Progress in Earth and Planetary Science (2026) 13:17
https://doi.org/10.1186/s40645-026-00804-z

Progress in Earth and Planetary Science

RESEARCH ARTICLE Open Access

Multi-technique SAR coseismic deformation retrieval and fault modeling of the 2025 Mw 7.7 Myanmar earthquake

Valerio Ruocco[1,2], Silvia Puliero[2*], Simone Atzori[2], Cristiano Tolomei[2], Andrea Antonioli[2], Marco Polcari[2], Matteo Albano[2], Marco Moro[2], Salvatore Stramondo[2], Michele Saroli[1,2], Pasquale Striano[3], Fernando Monterroso[3], Manuela Bonano[3], Francesco Casu[3], Claudio De Luca[3] and Riccardo Lanari[3]

Abstract

This study investigates the coseismic displacement field caused by the Mw 7.7 earthquake that struck Myanmar on March 28, 2025, along a segment of the Sagaing Fault, a well-known, right-lateral strike-slip fault. To such a purpose, a combination of satellite synthetic aperture radar (SAR)-based techniques, specifically Pixel Offset Tracking (POT), Multiple Aperture Interferometry (MAI), and SAR interferometry (InSAR), was applied to multiple Sentinel-1 SAR images covering the broad region affected by the seismic event. The retrieved deformation measurements were subsequently inverted using an analytical model to reconstruct the geometry and key parameters of the seismogenic source. In addition, a Coulomb Failure Function (CFF) analysis was performed to assess the stress transfer from the mainshock to the Mw 6.7 aftershock and determine the positive correlation between the two subsequent events. The results revealed a rupture extending approximately 490 km across three distinct fault segments, with a nearly vertical, north–south orientation and predominantly right-lateral strike-slip mechanism, in agreement with the regional tectonic setting. This comprehensive analysis offers key insights into the rupture extent and the mechanics of the major seismic event.

Keywords Myanmar earthquake, InSAR, Seismic source modeling, CFF

1 Introduction

At 06:20 UTC (12:50 local time) on 28 March 2025, a major earthquake of Mw 7.7 occurred in central Myanmar, along a segment of the NS-oriented Sagaing Fault, a right-lateral strike-slip fault. The epicenter was located approximately 16 km west of Mandalay, Myanmar's second-largest city, and 14 km north–northwest of Sagaing city. The shallow rupture, whose hypocenter is located at a depth of roughly 10 km, generated intense ground shaking (Modified Mercalli Intensity IX) in densely populated urban centers such as Mandalay, Sagaing, and Naypyidaw. The impact in terms of human casualties and infrastructure damage was severe, with over 4900 fatalities, approximately 6000 injuries, and widespread structural damage reported, including destruction of buildings and transportation infrastructure (airports, roads, and bridges). Furthermore, the seismic energy released during the event was efficiently transmitted over long distances, with perceptible effects reported more than 1000 km from the epicentral area. In Bangkok (Thailand), the collapse of a high-rise building is likely attributable to local seismic amplification associated with the geological setting, specifically the presence of predominantly loose,

*Correspondence:
Silvia Puliero
silvia.puliero@ingv.it
[1] DICeM - Università Degli Studi Di Cassino E del Lazio Meridionale, Cassino, Italy
[2] Istituto Nazionale Di Geofisica E Vulcanologia, Rome, Italy
[3] Istituto Per Il Rilevamento Elettromagnetico Dell'Ambiente, Consiglio Nazionale Delle Ricerche (IREA-CNR), Naples-Milan, Italy

unconsolidated sedimentary deposits (Shahzada et al. 2025).

The mainshock was followed at 6:32 UTC by a significant aftershock of Mw 6.7, whose epicenter was located about 34 km SSE of the mainshock. Furthermore, between March 28 and April 17, the area was struck by numerous aftershocks with magnitudes ranging from 4.1 to 5.3. The Mw 5.3 aftershock was recorded on April 13 at 2:24 UTC, approximately 34 km NNE of the city of Meiktila and about 94 km from the mainshock (USGSa 2025).

The rupture propagated over approximately 90 s at a speed of about 5 km/s, affecting a 460–480 km-long segment of the Sagaing Fault, which is one of the longest, straightest, and most active and hazardous strike-slip faults in Southeast Asia (Bradley & Hubbard 2025; Vera et al. 2025). This unexpected rupture length suggested the occurrence of a supershear earthquake, a rare event where the rupture propagates along the fault plane (in a southerly direction, in this case), moving faster than the average shear wave speed (S-waves), resulting in a shock wave produced by the cumulative interference of S-waves emitted at different stages of rupture propagation. This dynamic can significantly amplify ground motion and contribute to more severe structural damage in the affected areas (Scarr et al. 2025). In fact, Vera et al. (2025), based on teleseismic data, confirmed that the rupture transitioned from subshear (0–32 s), with a velocity of ~3 km/s (Wei et al. 2025), to supershear (33–78 s), achieving a maximum velocity of > ~5.3 km/s (around 50 s) due to the acceleration in the southern segment, within the seismic gap of the Sagaing Fault where significant elastic strain had concentrated. Additional evidence for the supershear rupture is provided by the atypically few M > 4 aftershocks, mainly along the southern rupture segment. This supershear event is analogous to the 2001 Kunlun and 2002 Denali earthquakes (Vera et al. 2025), characterized by rupture velocities exceeding 5 km/s (Walker & Shearer 2009), and to the 2023 Türkiye supershear earthquake (M 7.8), which generated a bilateral rupture of comparable length, approximately 500 km (Petersen et al. 2023), and exhibited similar rupture velocities, particularly along the northeastward segment, attaining ~ 5.2 km/s (Zeng et al. 2025).

The aim of this study is to retrieve the seismogenic source of the Myanmar earthquake, including its fault geometry and slip distribution, derived through inverse modeling of the coseismic surface displacements. The inverse modeling was performed using multiple Sentinel-1 datasets derived from different Synthetic Aperture Radar (SAR)-based techniques, to account for the predominantly north–south orientation of the fault. Specifically, the analysis considered the results integrated from Pixel Offset Tracking (POT) (Gray et al. 1998), Multiple Aperture Interferometry (MAI) (Bechor & Zebker 2006), and conventional two-pass interferometric SAR (InSAR) (Massonnet et al. 1993) to enhance sensitivity to displacement components. Furthermore, the Coulomb Failure Function (CFF) was computed to evaluate the cause-and-effect correlation between the Mw 7.7 mainshock and the subsequent Mw 6.7 event.

2 Tectonic settings

Myanmar is located within a complex tectonic collision zone between the southeastern margin of the Eurasian Plate and the Indian Plate. This geodynamic setting is characterized by a network of north–south trending faults that cross central Myanmar, accommodating and distributing the lateral northward displacement of the Burma Microplate relative to the Sunda Plate. Myanmar can be geographically subdivided into an eastern sector, dominated by the Shan Plateau, and a western sector, corresponding to the Burma Plate, which includes the Indo-Burman Ranges (IBR) and the Central Myanmar Basin (MCB) (Mitchell et al. 2012; Tha Zin Htet Tin et al. 2022) (Fig. 1).

The focal mechanism of the mainshock is consistent with this tectonic regime and compatible with rupture along the Sagaing Fault. This fault is a major right-lateral strike-slip structure, approximately 1200 km long and oriented north–south, extending from the Andaman Sea in the south to the southeastern Himalayas in the north, characterized by a pronounced linear geometry extending for approximately 700 km between latitudes 17°N and 23°N. The Sagaing Fault accommodates roughly 18–20 mm/year of the relative motion between the Burma and Sunda Plates, which is estimated at 35–36 mm/year (Socquet et al. 2006; Tha Zin Htet Tin et al. 2022; Vigny et al. 2003; Wang et al. 2014; Xu et al. 2025).

Applying the geomorphological and seismological approach proposed by Wang et al. (2014), the fault can be divided into six segments from south to north, with a potential Mw of 7–8 (Fig. 1): Bago Segment (~ 170 km), Pyu Segment (~ 130 km), Nay Pyi Taw Segment (~ 70 km), Meiktila Segment (~ 220 km), Sagaing Segment (~ 170 km), Northern Segment (~ 350 km). The Sagaing Segment, whose northern limit lies at approximately 23.5°N, is located where the fault splits into multiple complex segments. The Northern Segment includes four distinct active fault zones that terminate sequentially from west to east between approximately 25°N and 27°N. Slip rates along the fault have been estimated at approximately 20 mm/year in the central sections (Sagaing and Meiktila segments), consistent with previous geological and geodetic studies in the region, and at about 15–16 mm/year along the southernmost portion of the

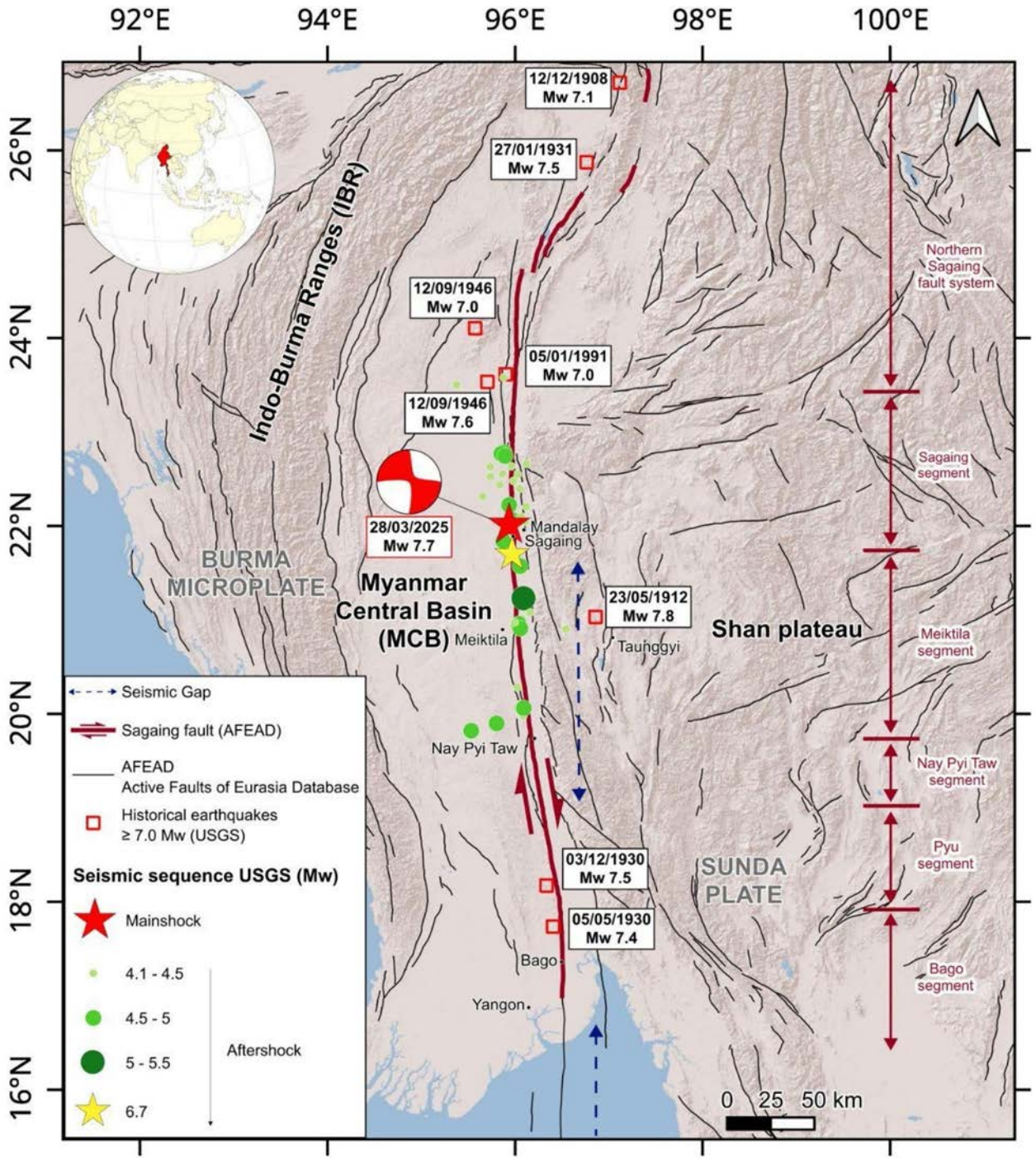

Fig. 1 Overview of the geographical setting and seismicity of the Myanmar area. The focal mechanism of the mainshock is shown together with the aftershocks and the historical earthquakes (USGSa 2025; USGSb 2025). The active faults are part of the Active Faults of Eurasia Database (AFEAD) (Zelenin et al. 2022). Fault segmentation is based on the classification proposed by Wang et al. (2014). The illustrated seismic gaps refer to the study by Hurukawa and Maung Maung (2011)

fault (Bago Segment). Furthermore, it is estimated that the potential magnitude of earthquakes along these segments is around 7.4 for the Meiktila Segment and 7.3 for both the Sagaing and Bago Segments (Tha Zin Htet Tin et al. 2022).

The mainshock occurred in a region that has experienced multiple large-magnitude events over the last

century. The Sagaing Fault, in particular, was responsible for eight earthquakes with Mw ≥ 7 starting from 1900 (USGSb 2025). According to Hurukawa & Maung Maung (2011), two seismic gaps were identified as zones with the potential to generate large future earthquakes. The first gap lies between 19.2°N and 21.5°N (corresponding to Meiktila Segment) in central Myanmar, with an estimated length of approximately 260 km and a potential maximum magnitude of 7.9. According to Bradley & Hubbard (2025), the Myanmar earthquake may represent a partial rupture of this long-recognized seismic gap. The second is located south of 16.6°N, in the Andaman Sea, with a length of around 180 km and a predicted magnitude of at least 7.7.

3 Materials and methods

The coseismic ground displacement field induced by the Mw 7.7 Myanmar earthquake was estimated using the POT (Gray et al. 1998), the MAI (Bechor and Zebker 2006), and the InSAR (Massonnet et al. 1993) techniques. The POT and MAI techniques were considered due to the significant north–south displacement component caused by the rupture along the Sagaing Fault and nearly undetectable with the conventional InSAR technique from near-polar orbiting satellites. To this aim, C-band Sentinel-1 SAR images acquired through the Interferometric Wide Swath (IWS) mode were exploited. Different tracks of Sentinel-1 data were collected along both ascending and descending orbits to cover the wide area affected by the coseismic deformation (Table 1).

3.1 Pixel Offset Tracking (POT)

In this study, we performed an investigation based on the POT technique (Casu et al. 2010) applied to the amplitude of the above-mentioned Sentinel-1 image pairs. This technique is based on the exploitation of the intensity information of the SAR images, and permits to estimate the 2D shifts between corresponding pixels in a pair of co-registered SAR images by maximizing the normalized cross-correlation (NCC) within a defined matching window. This allows us to retrieve the displacement maps along both range and azimuth directions. Since the POT displacement measurements depend mainly on the SAR images ground resolution, which is 5 m in range and 20 m in azimuth for Sentinel-1 at full resolution, it is possible to achieve an accuracy level of the displacement maps of about 0.5 m and 2 m, respectively, in range and azimuth, according to the estimate of about 1/10 of the resolution proposed by Casu et al. (2011). The outcomes were geocoded at a spatial resolution of 30 m.

3.2 Multiple Aperture Interferometry (MAI)

The MAI technique exploits the SAR interferometry principle applied to subapertures of the antenna beam to constrain any displacement that occurs along the azimuth direction, which is approximately the NS direction due to the quasi-polar orbits followed by the SAR sensors. In particular, two interferograms are estimated along the azimuth direction by forward and backward shifting the radar squint angle, and the azimuth displacement is estimated from the difference between the two. Indeed, considering θ as the radar nominal squint angle and β as a small squint-angle shift, the forward-looking interferogram is retrieved by using a radar squint angle slightly greater than the nominal one, $\theta+\beta$, and vice versa for the backward-looking interferogram (θ-β).

Then, the forward and backward interferograms can be expressed as:

$$\varphi_{Forward} = \frac{-4\pi\,\Delta x}{\lambda} sin\left(\theta_{SQ} + \beta\right) + \varphi_{top} + \varphi_{err}$$

$$\varphi_{Backward} = \frac{-4\pi\,\Delta x}{\lambda} sin\left(\theta_{SQ} - \beta\right) + \varphi_{top} + \varphi_{err}$$

where λ is the radar wavelength, Δx is the displacement along the azimuth direction, ϕ_{top} represents the topographic phase, and ϕ_{err} includes all the noise contributions. The azimuth displacement is estimated by subtracting the two phases:

Table 1 Characteristics of the SAR images and the respective applied techniques (AZ = azimuth, RG = range)

Orbit pass	Track	Interferogram pair	Technique	Incidence angle (°)	Perpendicular baseline (m)
Ascending	70	March 22, 2025 April 03, 2025	POT (RG/AZ) MAI InSAR	39	19.5
	143	March 27, 2025 April 08, 2025	POT (RG/AZ)	39	23.5
Descending	33	March 19, 2025 March 31, 2025	POT (RG/AZ)	39	96
	106	March 24, 2025 April 05, 2025	POT (RG/AZ) MAI InSAR	39	160

$$\varphi_{MAI} = \varphi_{Forward} - \varphi_{Backward} = \frac{-4\pi\,\Delta x}{\lambda} 2sin(\beta)cos(\theta_{SQ}) \approx \frac{2\pi}{L}\Delta x$$

where L is the antenna length. Here, the MAI technique was applied to two pairs of Sentinel-1 ascending and descending data (see Table 1). Forward, backward interferogram was estimated by applying multilook factors of 24 by 6, thus reaching a pixel spacing of the displacement maps of about 90 m. The final outcomes, i.e., the azimuth displacement maps, were geocoded using the 30-m DEM acquired by the SRTM mission. The following technique achieves centimetric accuracy (Bechor and Zebker 2006; Jiang, et al. 2017).

3.3 InSAR technique

Being the Sagaing Fault oriented along the north–south direction, with a strike-slip regime, most of the deformation is along horizontal axes, with the main deformation component occurring along the N-S direction that can be underestimated by the InSAR technique due to the quasi-polar orbits of the satellite. Nevertheless, the InSAR technique was still profitably applied to measure the coseismic deformation to derive other potential displacement components. We generated coseismic interferograms by removing the topographic component using the 30-m resolution ALOS World3D digital elevation model (Takaku et al. 2020). To minimize interferometric phase noise, an adaptive filtering technique was applied (Goldstein & Werner 1998). The resulting phase was then unwrapped using the minimum cost flow method (Costantini 1998), and the data were geocoded at a spatial resolution of 30 m. The outcomes provided by the InSAR technique are maps showing displacement along the LoS with centimetric accuracy (Massonnet & Feigl 1998).

3.4 Source modeling

The modeling of the source for the Mw 7.7 earthquake in Myanmar was carried out using a two-step approach consisting of a nonlinear least-squares optimization to determine the location (latitude and longitude), depth, dimensions (length and width), orientation (strike and dip angles), and rupture mechanism and intensity of the source (9 parameters for each source segment), followed by a linear inversion to reconstruct the slip distribution and direction along the fault. The source model adopted is the finite fault dislocation in an elastic half-space proposed by Okada (1985), modified to include topographic contributions following the approach of Williams & Wadge (1998) to obtain a more realistic estimate of the source depth. In addition to the source parameters, orbital ramp parameters for the InSAR datasets and a rigid offset for the POT and MAI data were also estimated.

With the nonlinear modeling process, the parameters of the three source segments, each characterized by uniform slip, are estimated. The nonlinear inversion employs the Levenberg–Marquardt algorithm (Marquardt 1963) to identify the global minimum, implemented with a series of restarts to avoid convergence toward local minima. Once the best-fit parameters are determined, the associated uncertainties are evaluated; in this phase, each dataset is artificially perturbed with ad hoc noise (spatially correlated in the case of all the datasets) and subsequently re-inverted through the same nonlinear procedure. Further details on the full nonlinear inversion process are provided in Atzori et al. (2009). To assess these sources, 500 inversions were performed: Best-fit values and uncertainties are reported in Table 2; histograms and scatter plots with parameter trade-offs and a 3D view of the sources derived from this analysis are shown in Figs. 2, 3, and 4.

From the values reported in Table 2 and Figs. 2–4, it is evident that the geometries of the source segments are well constrained by the datasets, though some trade-offs (like the usual one between slip and width) are present. The 3D graphical representation of the "cloud of solutions" coming from the 500 inversions also provides an effective visualization of the robustness of the inversion-derived solution.

The linear inversion was conducted using the "full-resolution" algorithm, which divides the fault surface into variably sized patches to ensure an almost complete resolving power on each individual element. The algorithm is based on the model resolution matrix, described in Atzori and Antonioli (2011), and is defined as $\mathbf{R} = \mathbf{G}^{-g} \cdot \mathbf{G}$, where $\mathbf{G}^{-g}$ denotes the generalized inverse of the linear system $\mathbf{d} = \mathbf{G} \cdot \mathbf{m}$, with $\mathbf{d}$ representing the

Table 2 Best-fit values after the nonlinear inversion, with their 1-sigma uncertainty within brackets

	Length [km]	Width [km]	Depth [km]	Dip [deg]	Strike [deg]	East [deg]	North [deg]	Rake [deg]	Slip [m]
segm. 1	115.8 (1.8)	12.3 (2.6)	−0.4* (0.3)	69.2 (5.2)	−0.7 (0.4)	96.005 (0.007)	22.044 (0.008)	−177.7 (1.4)	3.98 (0.62)
segm. 2	140.3 (2.5)	10.5 (1.4)	0.0 (0.1)	72.7 (3.3)	−4.4 (0.1)	96.054 (0.003)	20.876 (0.012)	−177.8 (1.2)	4.44 (0.39)
segm. 3	186.4 (3.3)	7.6 (1.5)	0.2 (0.2)	88.2 (3.6)	−8.6 (0.2)	96.222 (0.003)	19.426 (0.015)	−178.5 (1.3)	4.72 (0.66)

* negative values correspond to depth above the sea level

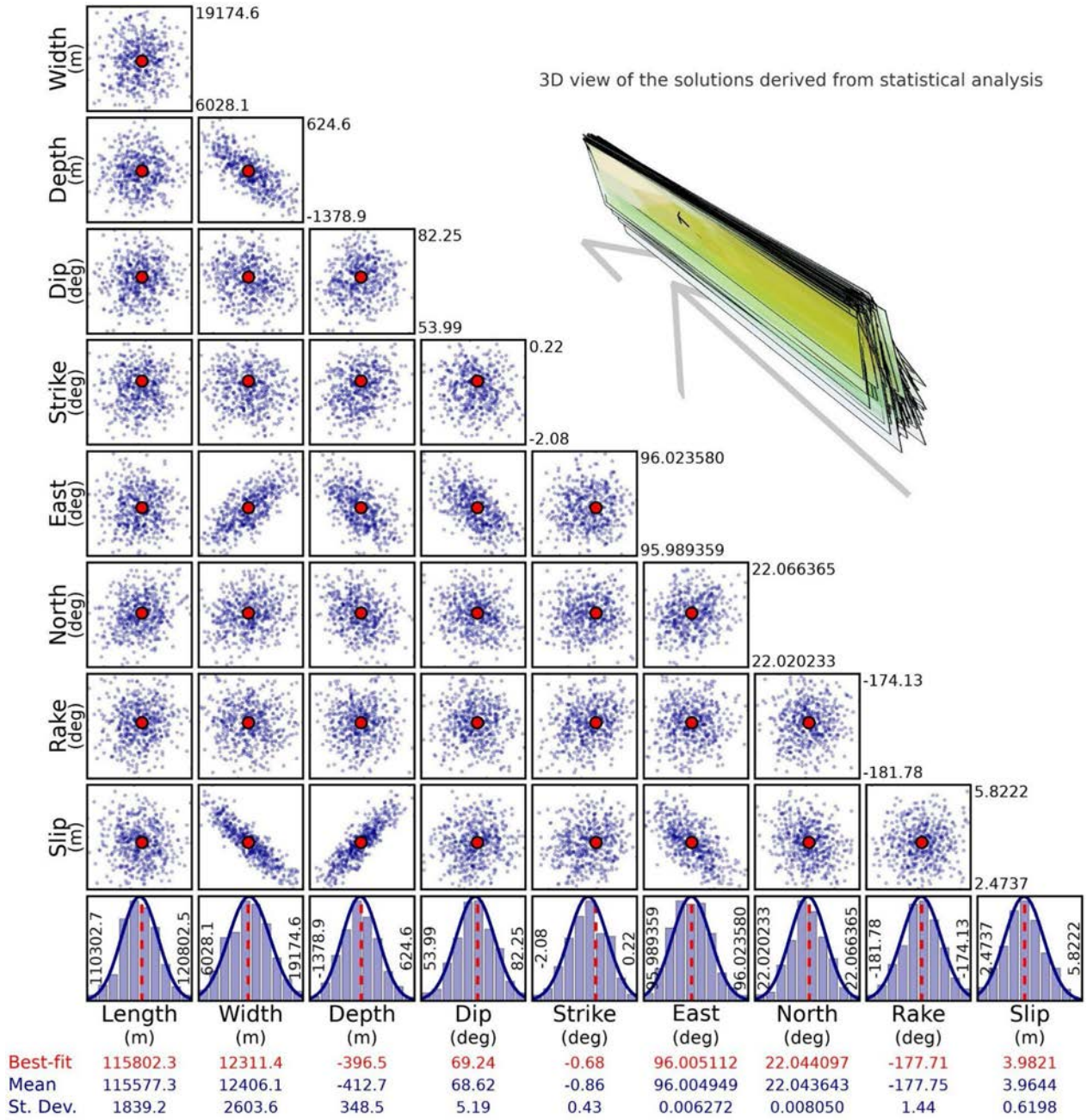

Fig. 2 Uncertainty analysis for Segment 1: best-fit values from the nonlinear inversion, along with the mean values and standard deviations obtained from the 50 nonlinear inversions performed for uncertainty estimation. The scatter plots illustrate possible trade-offs among the parameters. The 3D figure is a graphical representation of the sources corresponding to each of the 500 solutions

array of observed data and **m** the model parameters, i.e., the slip values.

In the model resolution matrix **R**, the diagonal values range from 0 to 1, thereby quantifying the degree to which each element is constrained by the data: 1 indicates a perfectly resolved parameter, whereas 0 denotes a completely unresolved one. For a comprehensive treatment, the reader is referred to Menke (1989). The *full-resolution* algorithm partitions the fault plane to maximize the resolution of each element, that is, maintaining the resolution matrix as close as possible to the identity matrix. During the iterative subdivision process, the fault is discretized into elements whose resolution values approach unity. Figure 5 illustrates the comparison

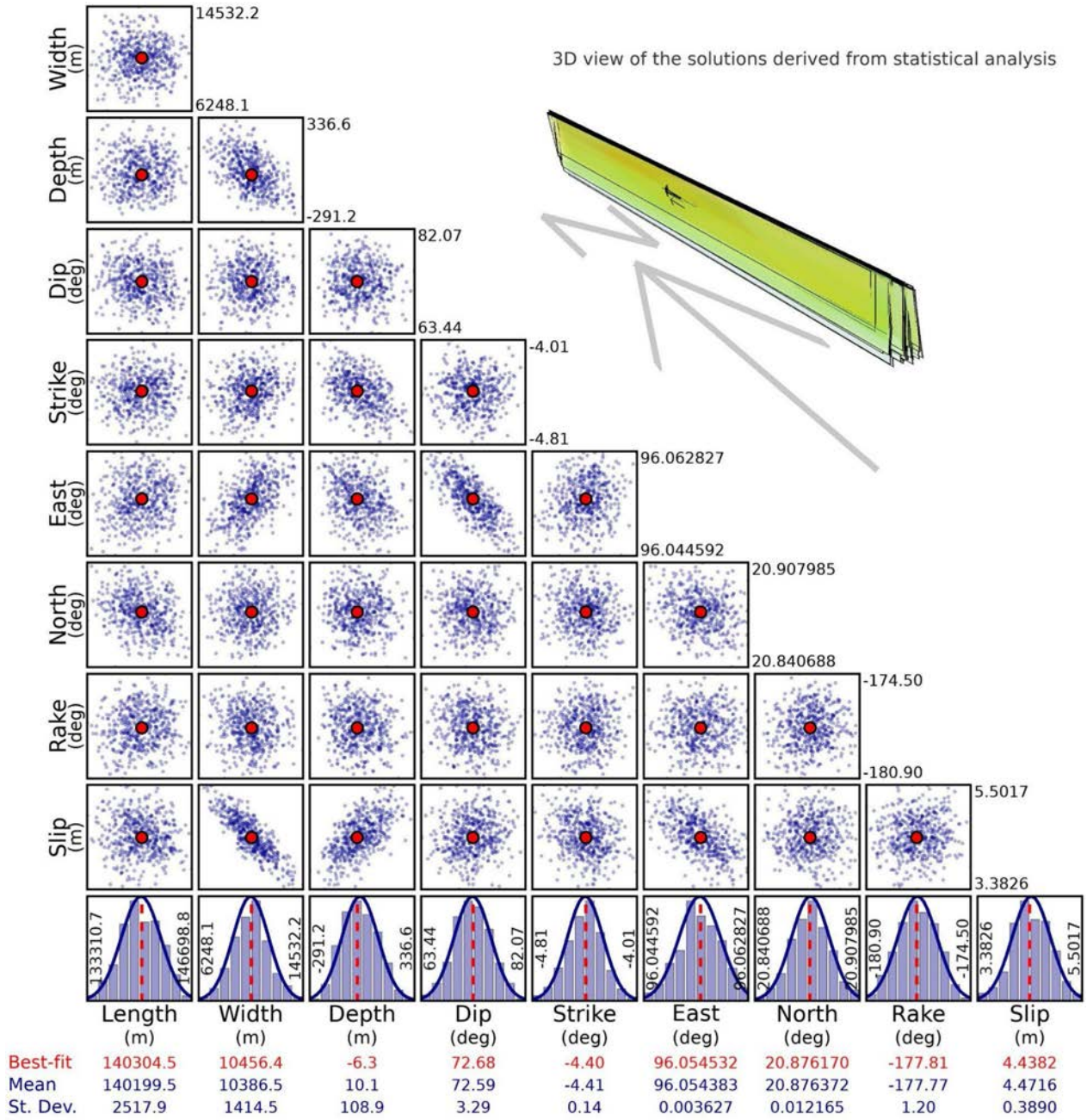

Fig. 3 Same as Fig. 2, referred to Segment 2

between the resolution values obtained with the *full-resolution* algorithm and those from a subdivision into predefined patches of equal size.

Compared to the typical subdivision into predefined-size patches, the "full-resolution" algorithm offers several advantages: (i) it inhibits oversplitting, i.e., the division into elements too small to be effectively constrained by data; (ii) it makes resolution tests such as the "checkerboard test" unnecessary; (iii) it reduces the importance of a priori regularization (damping of the slip distribution); (iv) it provides more robust uncertainty estimates by minimizing off-diagonal terms in the variance–covariance matrix of the estimated parameters; (v) it ensures the best fit of the observed data using the minimum number of parameters.

All of these advantages are discussed in Atzori et al. (2019) and are particularly relevant in the case of nearly vertical faults like the one analyzed here, for which the

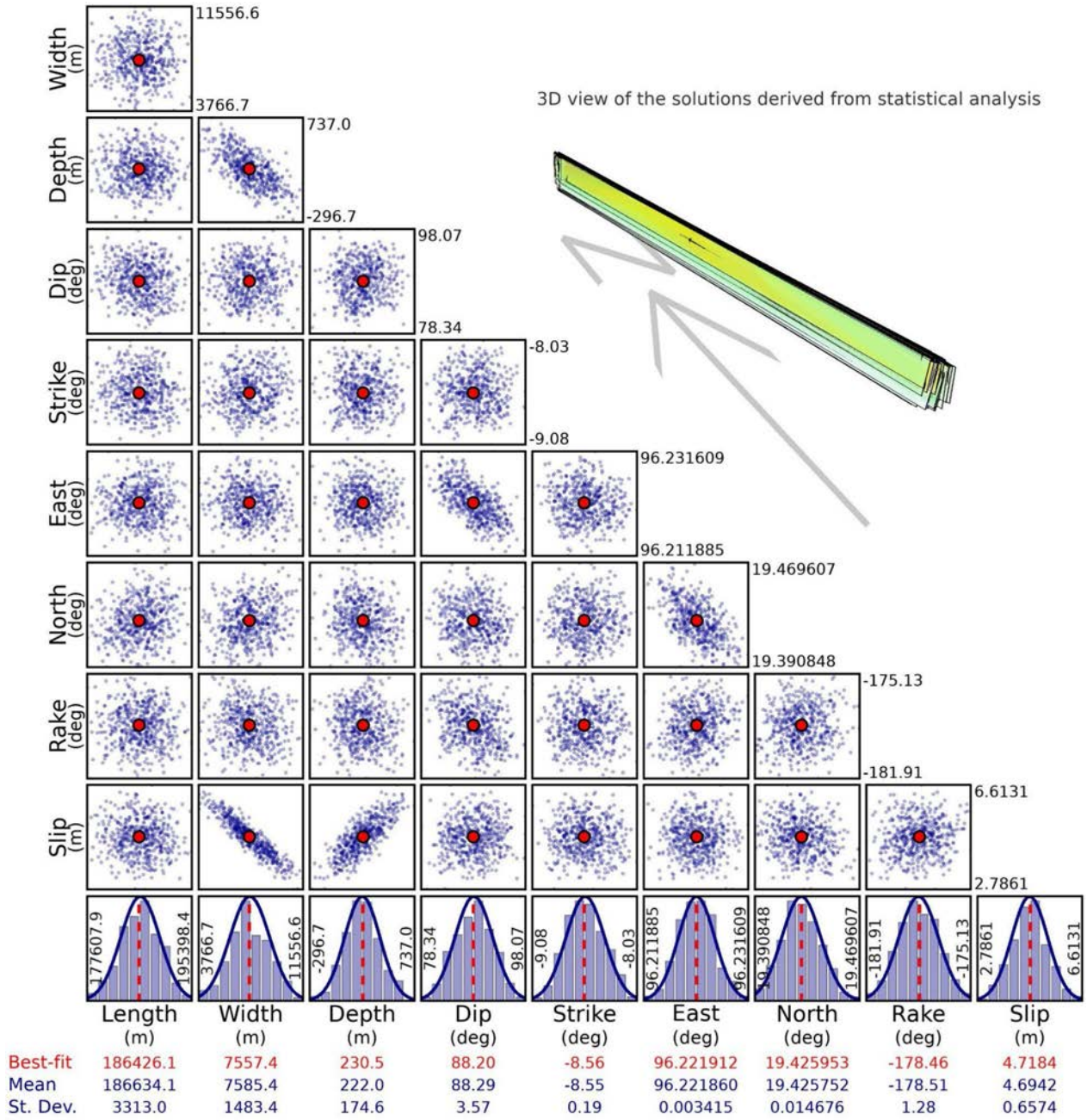

Fig. 4 Same as Fig. 2, referred to Segment 3. It must be noted that, since the fault is nearly vertical, some of the sources of the 500 tests have a dip in the opposite direction, corresponding to the swap between hanging wall and footwall. In the graphs, these solutions are shown with dip > 90°, forcing the convention of a dip range (0°–90°), solely for graphical continuity; according to convention, this subset of solutions should have dip < 90°, the strike rotated by 180° and a rake mirrored with respect to the horizontal

resolving power of the observed data decreases rapidly with depth.

Since InSAR, POT, and MAI data are characterized by very different uncertainties, both inversions were conducted by assigning weights to each dataset based on an analysis of the cost function derived from the chi-squared statistic; the criterion for assigning a proper weight to each dataset is described in Atzori et al. (2019).

The use of displacement data derived from different techniques entails uncertainties that can vary significantly. This condition provides the opportunity to recall the methodology employed to balance the datasets in

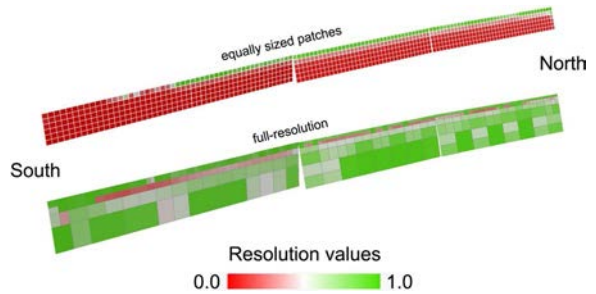

Fig. 5 Distribution of resolution values, extracted from the diagonal of the model resolution matrix, for a subdivision into equally sized patches of 4 km and for that derived from the *full-resolution* algorithm

the inversion (both nonlinear and linear). For a comprehensive discussion, reference can be made to Atzori et al. (2019). The datasets used in this study were initially introduced into the inversion with an assigned uncertainty (1-sigma) of 0.02 m for InSAR data, 0.25 m for MAI, and 0.5 m and 2 m for offset tracking in the range and azimuth directions, respectively, corresponding to 1/10 of the resolution in each direction.

During the inversion, we minimize the following cost function, which is the total of the cost functions $CF(D)$ of every dataset:

$$Costfunction = \sum CF(D) = \sum_{D} \left(\frac{W_D}{N_D} \bullet \sum (e_D^T W_{e,D} e_d) \right)$$

where, for every dataset D, the vector $\mathbf{e}$ contains the point-by-point difference between observed and predicted values, N is the number of observations, $\mathbf{W}_e$ is a data weighting matrix for the single dataset, and w_D is a dataset weighting coefficient. Actually, $\mathbf{W}_e$ is the inverse of the full variance–covariance matrix Cov($\mathbf{d}$) of the observed data $\mathbf{d}$ for InSAR data, while for the other techniques, the covariance is not considered, and $\mathbf{W}_e$ is a diagonal matrix with the inverse of the data variance, using the sigma values reported above. The weighting coefficient w_D is initially assumed equal to 1.

In a purely theoretical case, for every dataset, we should have that.

$$CF(D)_{theor} = \frac{1}{N} \cdot \sum \left(e^T W_e e \right) = 1$$

but in practice, $CF(D)$ is always $\neq 1$, due to the impossibility of a formal assessment of Cov($\mathbf{d}$) and, as a consequence, of $\mathbf{W}_e$. After the first inversion, w_D is calculated to have $CF(D) \cdot w_D = CF(D)_{theor} = 1$. A second inversion is then run, introducing w_D as the stretching factor of Cov($\mathbf{d}$), according to

$$Cov(d)_{new} = \frac{1}{W_D} Cov(d)$$

A new solution is then obtained, with different residuals and a new assessment of w_D, which is in turn used as the uncertainty stretching factor in the next iteration; in a few iterations, w_D values get stable, and the cost function contribution of every dataset is perfectly balanced.

The final values of the coefficients w_D, together with other information related to the inverted datasets, are reported in Table 3.

The inversion process was carried out using a set of points sampled from the 12 SAR-based datasets, totaling approximately 70,000 observations, with resolutions of 2 km and 5 km for the near- and far-field, respectively.

Table 3 Summary of selected parameters of the datasets used in the inversion: orbital direction (ascending/descending), technique employed to measure displacements (AZ = azimuth, RG = range, POT = Pixel Offset Tracking, MAI = Multiple Aperture Interferometry), number of inverted samples, parameter w_D for dataset weighting, RMS of the residuals, and RMS of the observed data (null solution)

Pair	Orbit pass	Technique	Samples	w_D	RMS residuals [m]	RMS null [m]
19MAR2025-31MAR2025	D	AZ POT	2069	9.78	0.459	0.787
22MAR2025-03APR2025	A	AZ POT	5785	2.38	0.941	1.329
24MAR2025-05APR2025	D	AZ POT	7118	2.15	0.993	1.295
27MAR2025-02APR2025	A	AZ POT	7462	10.19	0.455	1.021
19MAR2025-31MAR2025	D	RG POT	1412	15.31	0.121	0.23
22MAR2025-03APR2025	A	RG POT	5755	9.78	0.143	0.169
24MAR2025-05APR2025	D	RG POT	6971	9.34	0.155	0.187
27MAR2025-02APR2025	A	RG POT	6644	33.79	0.082	0.118
22MAR2025-03APR2025	A	MAI	5385	0.27	0.425	0.808
24MAR2025-05APR2025	D	MAI	6215	0.35	0.378	0.773
22MAR2025-03APR2025	A	InSAR	5505	0.17	0.049	0.048
24MAR2025-05APR2025	D	InSAR	7102	0.08	0.036	0.135

Although the fault trace, reaching the surface and clearly visible in the displacement maps, is nearly straight and oriented north–south, the rupture was modeled using three segments to allow the retrieved source to better follow the slight deviations from a purely linear feature. During the nonlinear inversion phase, all the parameters of the three segments (i.e., 27 parameters in total) were left unconstrained and simultaneously retrieved; moreover, the best-fit values reported in Table 2 indicate that the subdivision into three segments accommodates the curvature of the surface trace. The linear inversion was then performed, allowing for variability in the rake angle, to account for potential small deviations from the best-fit value obtained in the nonlinear inversion. For completeness, see Atzori et al. (2019) for an analysis of the performance of the "full-resolution" algorithm in the case of variable rake inversions.

3.5 Coulomb Failure Function (CFF) analysis

The variation of static stress (ΔCFF) generated by natural events can influence the timing of subsequent earthquakes (Harris 1998). To analyze the effect of the mainshock on the triggering of the Mw 6.7 event, which struck 12 min later, we computed the static ΔCFF on the aftershock plane. The calculation was based on fault parameters provided by USGS (USGSc 2025), selecting the plane consistent (strike 177°, dip 56°, and rake −170°) with the mainshock rupture geometry and was carried out following the definition:

$$\Delta CFF = \Delta\tau + \mu\prime\Delta\sigma$$

where μ'=μ (1-β) is the effective friction coefficient, μ is the coefficient of friction, and β is the Skempton parameter (Simpson & Reasemberg 1994; Stein et al. 1992). Δτ is the shear stress, and Δσ is the normal stress change, and the latter is assumed positive for extension. We adopt a value of 0.4 for the apparent friction coefficient. We have computed the six components of the induced stress tensor from which we calculated the normal, shear, and Coulomb stress changes caused by the first subevent on the second subevent fault plane, as discussed in the next section.

4 Results and discussion

The resulting Sentinel-1 coseismic ascending and descending displacement maps show the extent of the surface deformation induced by the earthquake, underscoring the intensity and the significance of the event. Thanks to the use of different techniques, the coseismic displacement field was constrained both along the azimuth and the range/Line of Sight (LoS) of the satellite. The POT and MAI techniques proved particularly effective in capturing the widespread displacements along the azimuth direction, consistent with the expected right-lateral strike-slip motion of the north–south-oriented Sagaing Fault (Fig. 6). In Fig. 6a–f, positive values correspond to ground movements in the azimuth direction, whereas negative values indicate movement in the opposite direction. These techniques well constrain coseismic slip, revealing a clear deformation offset across the Sagaing Fault, with maximum values up to 5 m observed along the fault trace, even at distant portions from the epicentral area, as highlighted by the transects crossing the fault (Fig. 6g, h).

The range/LoS displacement obtained from POT and InSAR techniques is shown in Fig. 7a–f. In this case, positive values represent deformations toward the satellite (reduction of satellite to ground distance) along the range/LoS, whereas a negative value indicates a deformation in the opposite direction. The analysis of multiple transects across the area of maximum displacements reveals values up to 0.7 m (Fig. 7g, h), likely indicating a combination of vertical, east–west, and a small percentage of north–south deformation components. The POT results, derived from amplitude-based image correlation, are consistent across all considered tracks and along both azimuth and range direction (Fig. 6a–d for azimuth and Fig. 7a–d for range), despite the rather low accuracy of the technique due to local noise resulting from the speckle effect and the limitations of Sentinel-1 azimuth resolution. The MAI analysis investigates the azimuth phase components only (Fig. 6e. f), yielding results that are in good agreement with those from POT (see cross sections in Fig. 6g, h) but providing higher measurement accuracy (Bechor and Zebker 2006). Conversely, while InSAR remains the standard technique for quantifying LoS displacements, its effectiveness is reduced by the predominantly north–south-oriented strike-slip mechanism of the Sagaing Fault. InSAR results are generally consistent with those from POT in the range direction, although the ascending-orbit cross section (Fig. 7g) reveals a slight difference in near-field range/LoS displacements. This is likely attributable to coherence loss near the fault, induced by the significant displacement. Nevertheless, the interferometric measurements still provide complementary value by capturing minor vertical displacements, potential east–west components, and by providing validation of the POT results along the range direction. InSAR contribution enhances the overall robustness of the displacement characterization when jointly interpreted with POT and MAI results.

To confirm the results of the Sentinel-1 processing, ALOS-2 ScanSAR interferograms were generated along both the ascending and descending orbits (Figure S1 in the Supplementary Material). The resulting displacement maps, however, exhibit some residual signals. Assuming

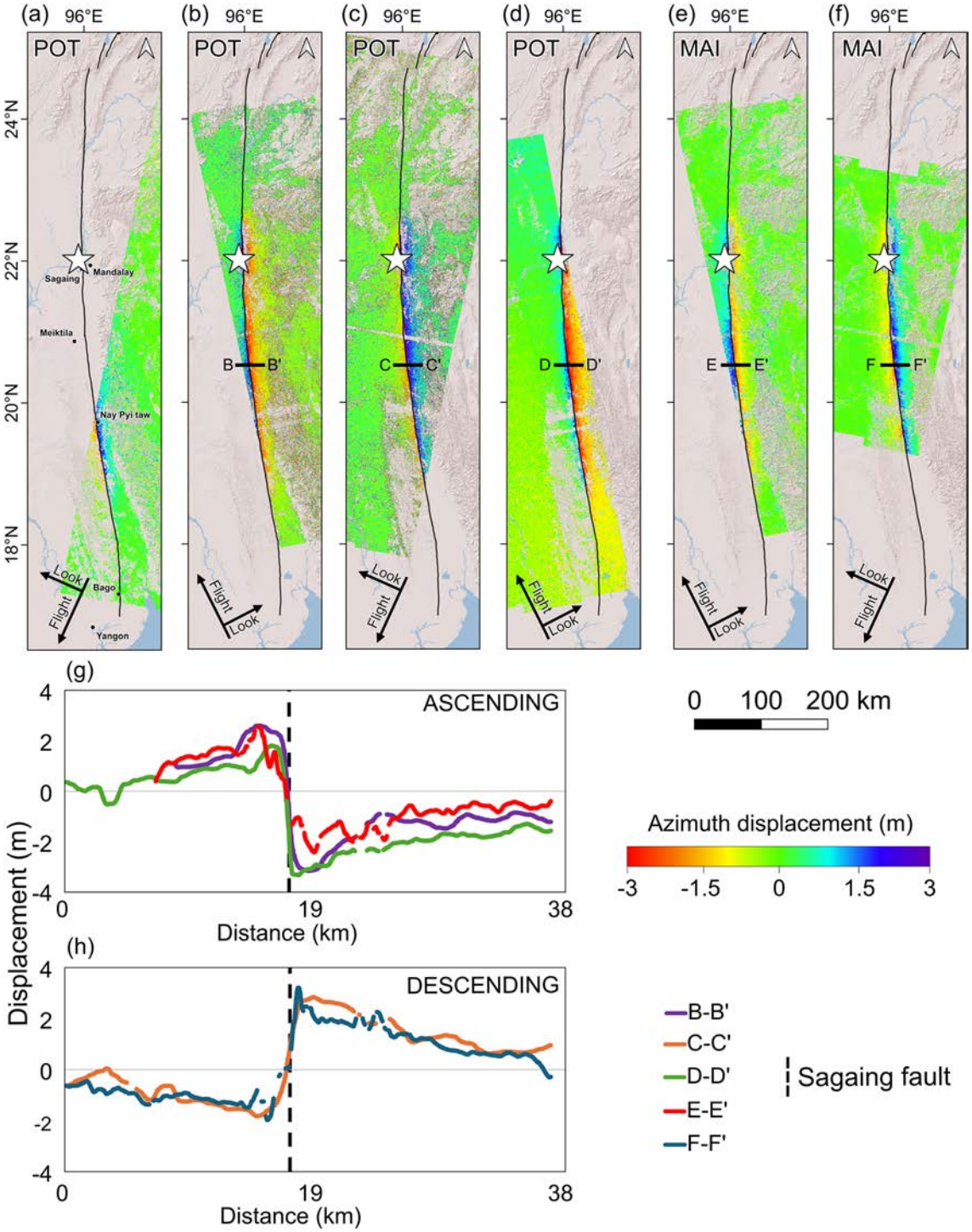

Fig. 6 Azimuth displacement map derived from the POT technique for **a** descending track 33, **b** ascending track 70, **c** descending track 106, **d** ascending track 143. Azimuth displacement map derived from the MAI technique for **e** ascending track 70 and **f** descending track 106. East–west profiles for each track along **g** ascending and **h** descending orbit are reported in correspondence with the area where the highest deformation was detected

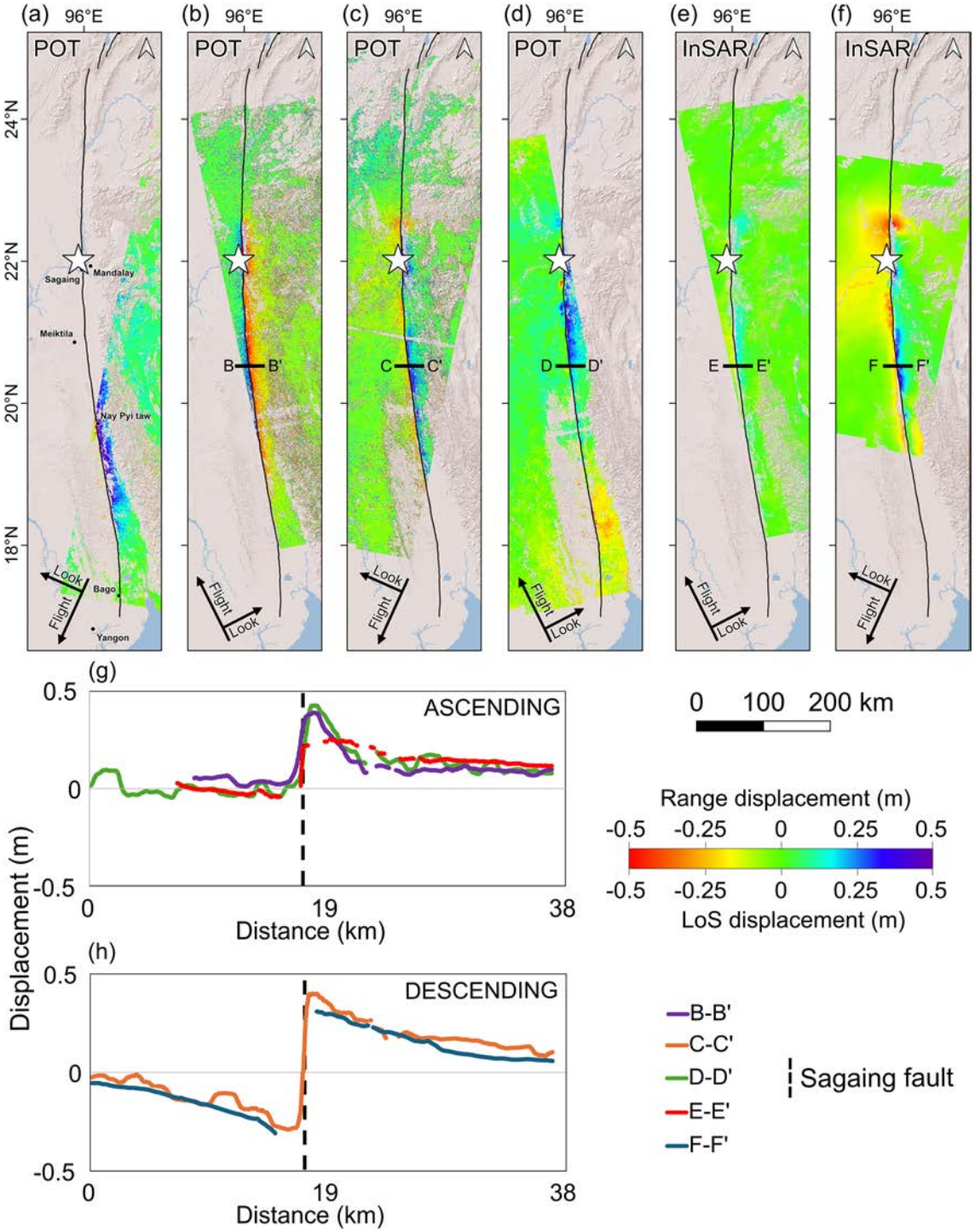

Fig. 7 Range displacement map derived from the POT technique for **a** descending track 33, **b** ascending track 70, **c** descending track 106, **d** ascending track 143. LoS displacement map derived from the InSAR technique for **e** ascending track 70 and **f** descending track 106. East–west profiles for each track along **g** ascending and **h** descending orbit are reported in correspondence with the area where the highest deformation was detected

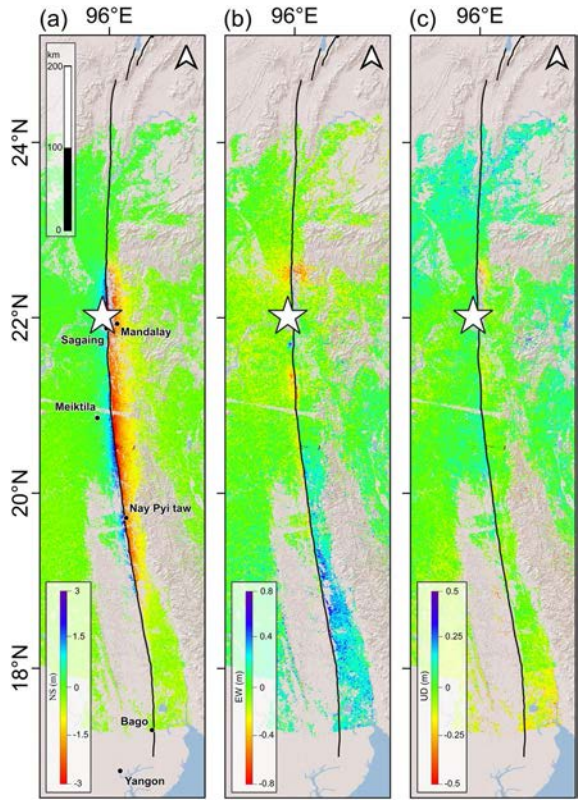

Fig. 8 Three-dimensional representation of coseismic surface deformation based on satellite data. These 3D deformation maps were derived from Sentinel-1 images acquired between March and April 2025 (see Table 1 for more details). **a** North–south direction deformation; **b** east–west deformation; **c** up–down deformation. The epicenter is indicated by the white star

comparable ionospheric conditions during the two acquisitions (Figure S2 in the Supplementary Material), ionospheric effects are expected to be secondary relative to other sources of uncertainty, such as orbital-related effects. For this reason, the obtained displacement maps were excluded from the source modeling inversion.

The 12 datasets were exploited and integrated to derive the three-dimensional coseismic displacement field along the north–south, east–west, and up–down components. The results (Fig. 8) confirm that the dominant deformation occurred in the north–south direction; however, significant contributions are also observed in the east–west component and a minor deformation along the vertical component. This highlights the importance of integrating multiple SAR techniques to achieve a comprehensive and robust characterization of the deformation field.

The obtained displacement maps in Figs. 6 and 7 were jointly inverted with the "full-resolution" algorithm described in the Materials and Methods section, enabling a robust retrieval of both the geometry of the seismogenic source responsible for the earthquake, as well as its slip distribution. The nonlinear inversion provided the geometry of the features involved in the coseismic slip, with the best-fit parameters (strike, dip, and rake) reported in Table 4. The uncertainties and trade-offs associated with such parameters are reported in the Materials and Methods section. Overall, the best-fit parameters are well constrained (Table 2 and Figs. 2, 3, and 4). The fault segments (Fig. 9a) show a north–south alignment along a nearly vertical dip with a faulting mechanism that is almost purely right-lateral for all three segments (Table 4), which is consistent with the tectonic regime of the area.

The slip distribution along the three fault segments has been constrained by linear inversion. In detail (Fig. 9), the maximum slip values of approximately 5 m are located in the central part of the fault segment number 2 (Fig. 9b), which corresponds to the portion of the Sagaing Fault affected by the seismic gap highlighted by Hurukawa and Maung Maung (2011) (Fig. 1). Moreover, the source modeling shows that the fault rupture is almost confined to the upper 15–20 km of the crust and extends over a length of approximately 490 km (Fig. 9). According to Thingbaijam et al. (2017), the expected rupture length for an Mw 7.7, strike-slip event should be approximately 300 km. In our case, the computed unusual extent of the fault slip distribution is explainable by invoking a supershear rupture, as already suggested by Melgar et al (2025), Vera et al (2025), Wei et al. (2025), and Xu et al (2025).

The comparison between the observed and modeled ground displacements is reported in Fig. 10 and 11, together with the residuals, showing a good agreement across all techniques and confirming the reliability of the SAR-based constraints and the robustness of the adopted modeling strategy.

Finally, the performed ΔCFF analysis in Fig. 12 reveals that the Mw 7.7 mainshock could have triggered the Mw 6.7 event, which happened 12 min later. Indeed, a strong positive static stress transfer, with values up to 1.9 MPa,

Table 4 Orientation, rupture mechanism, and seismic moment release for the three segments into which the source is modeled. The overall moment, magnitude, and focal mechanism are also reported

Name	Strike	Dip	Rake	Moment (N*m)
Segment 1	−0.7°	69.2°	−177.7°	1.70E + 20
Segment 2	−4.4°	72.7°	−177.8	1.95E + 20
Segment 3	−8.6°	88.2°	−178.5°	1.99E + 20
			Overall	5.65E + 20
			Magnitude	7.8
			Focal mechanism	

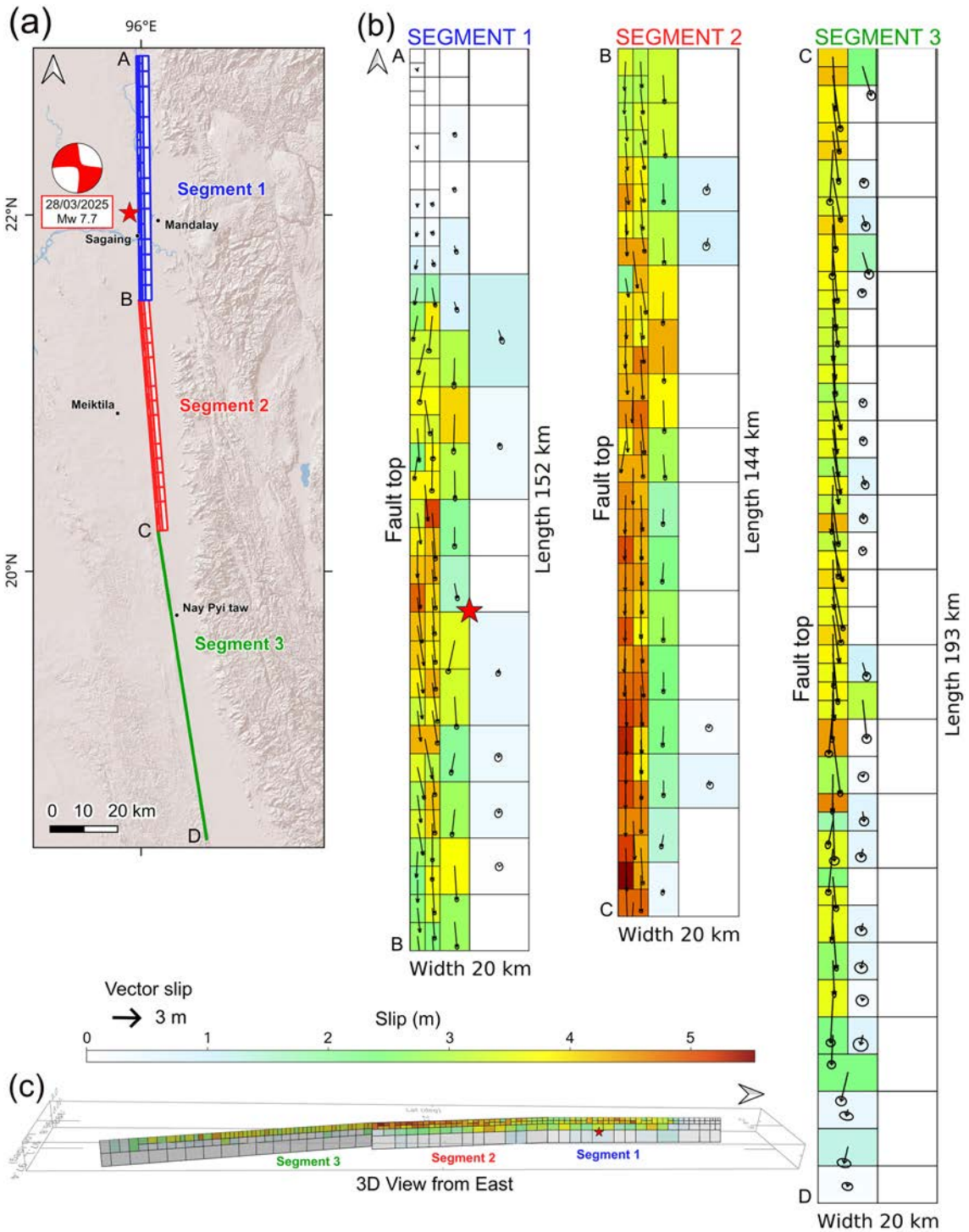

Fig. 9 Modeling of the three segments with the corresponding slip distribution derived from the inversion of InSAR data. **a** The 2D map view; **b** the slip distribution of each segment, in the strike/dip reference system, with associated 1-sigma uncertainties, represented by ellipses for each cell; **c** the 3D view from the east

is clearly observed on the receiver fault (Fig. 12). This suggests a positive correlation between the two events of the sequence, thus providing possible evidence of a causal link between the two ruptures. The temporal proximity between events further supports the hypothesis of stress interaction. This result supports the hypothesis that the

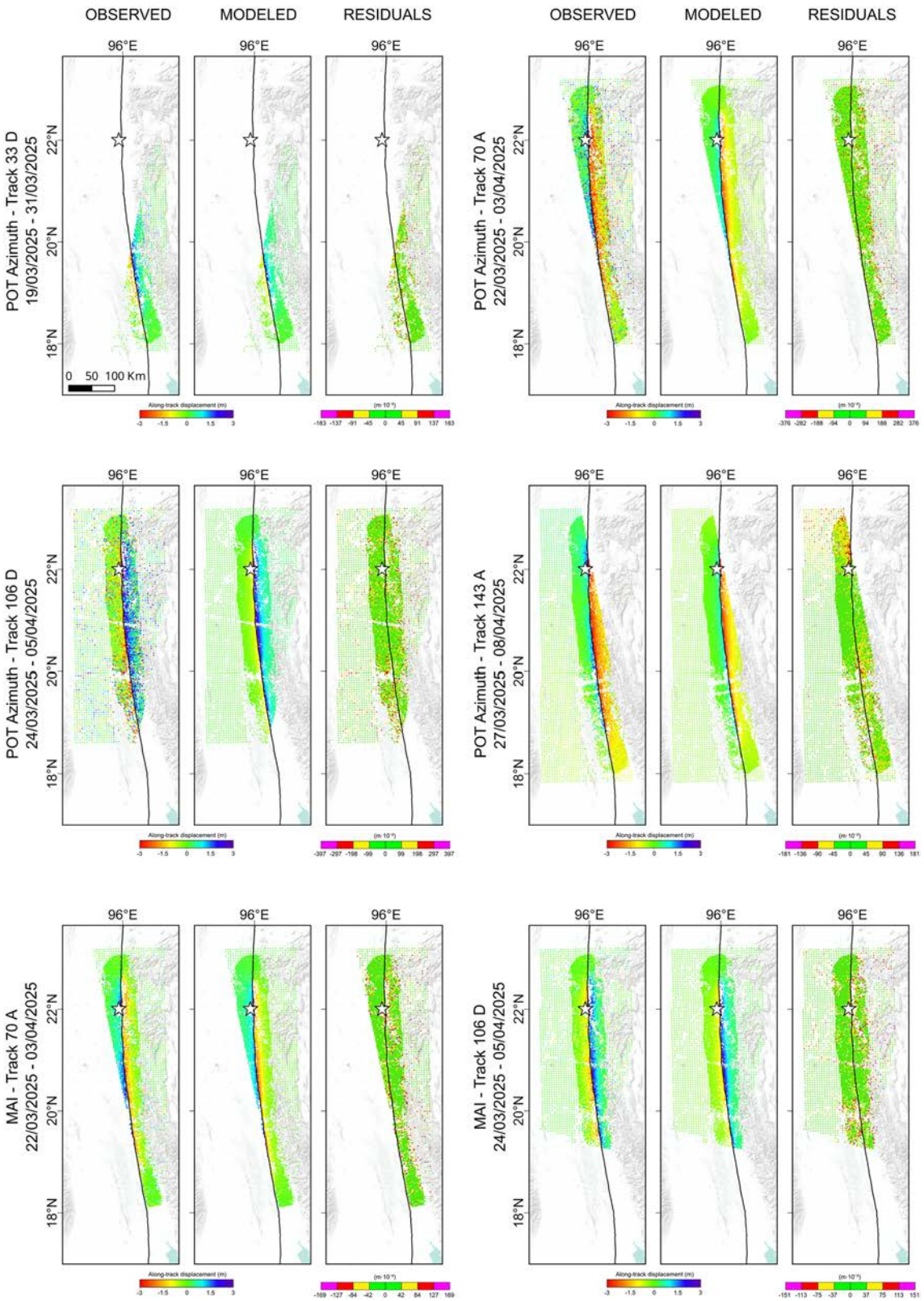

Fig. 10 Comparison between observed and modeled data for POT and MAI techniques along the azimuth direction. For each technique, the residual is also displayed

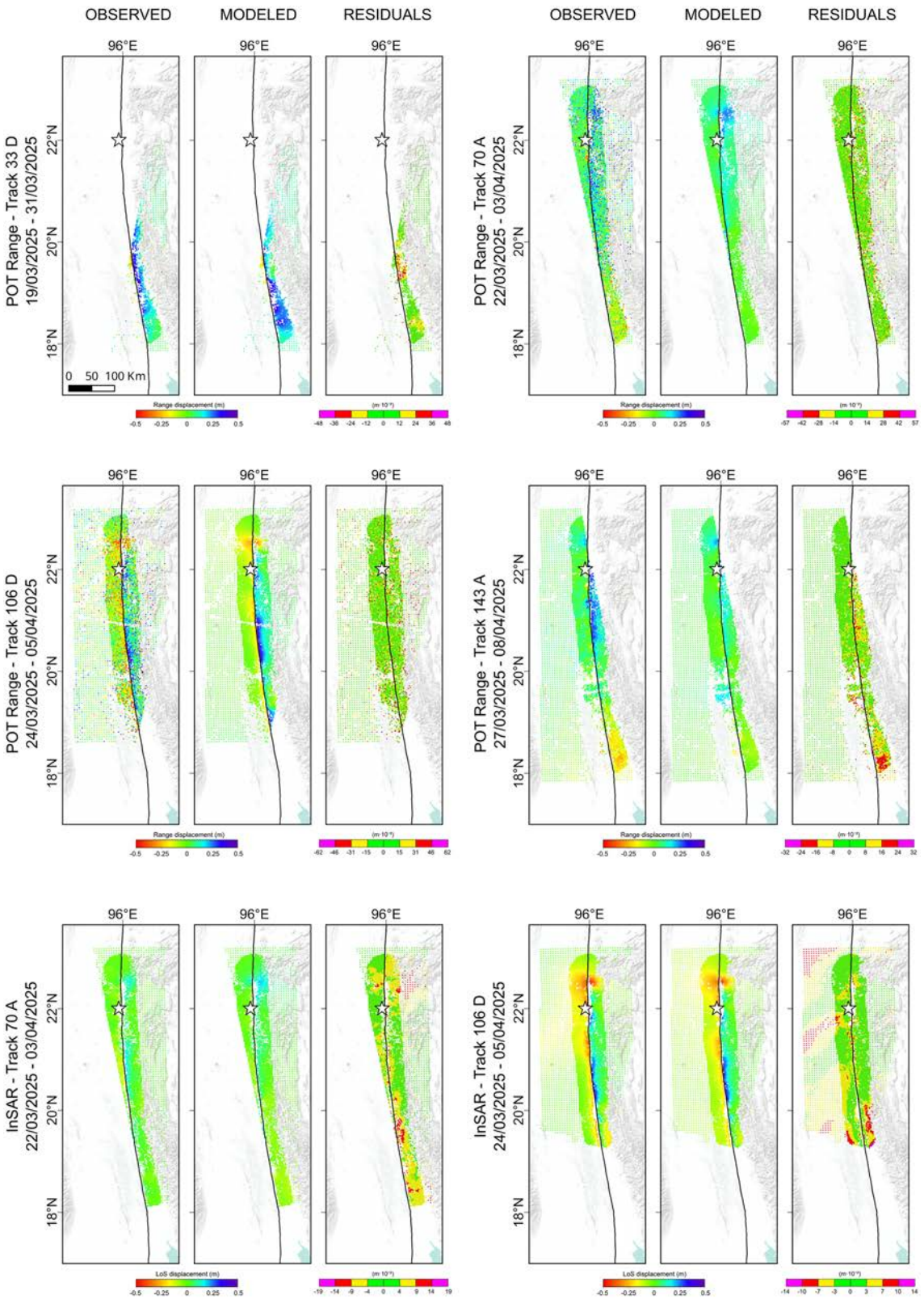

Fig. 11 Comparison between observed and modeled data for each technique along the range and LoS directions. For each technique, the residual is also displayed

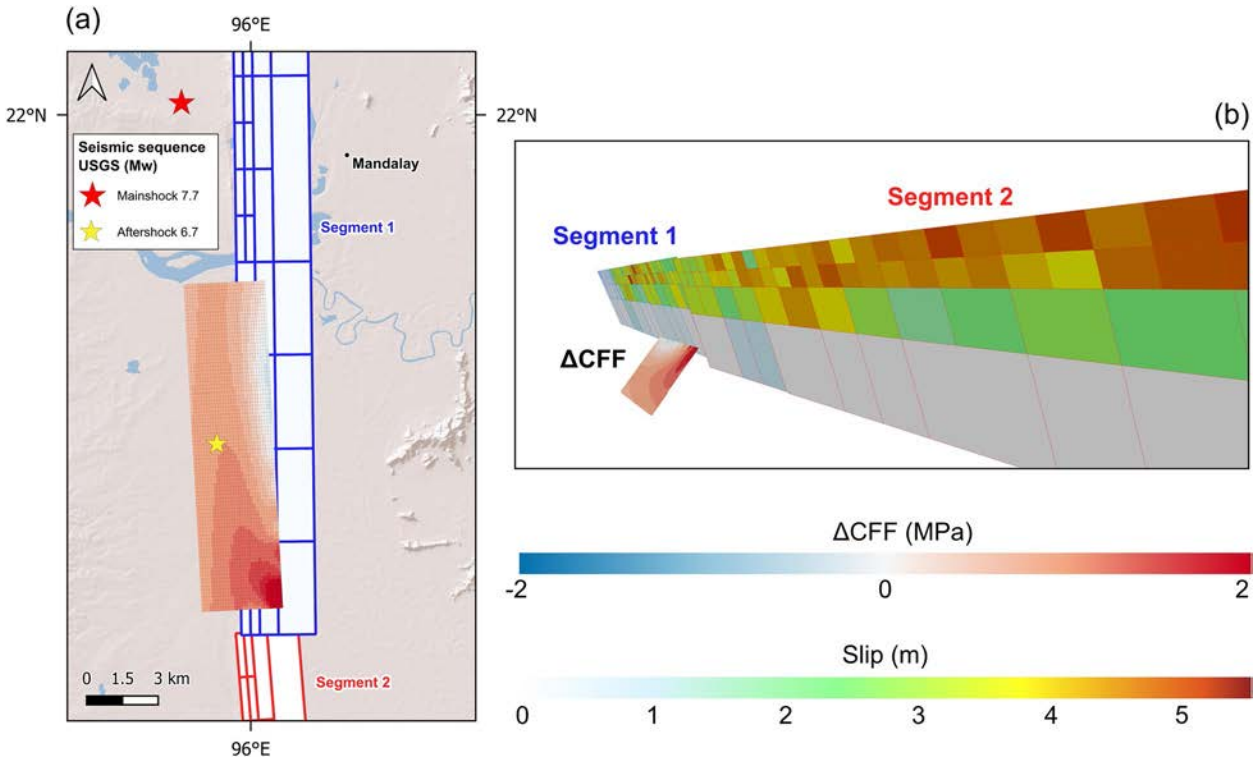

Fig. 12 **a** 2D view of the ΔCFF variation induced by the main event onto the 6.7 aftershock. The subevent fault plane is strongly loaded. **b** 3D view of the ΔCFF

Mw 6.7 aftershock was triggered by static stress changes induced by the mainshock through rupture propagation and stress concentration along the fault system.

5 Conclusions

The 2025 Mw 7.7 Myanmar earthquake was one of the most significant seismic events in Southeast Asia over the past century. Our analysis indicates that the rupture extended approximately 490 km along the Sagaing Fault, with a maximum coseismic slip of about 5 min the central part of the fault, consistent with a supershear rupture type. Overall, this study highlights the effectiveness of integrating multiple SAR techniques, each characterized by a different level of sensitivity and accuracy, for accurately capturing the full deformation field associated with such a strong earthquake over a wide area. This approach enabled the retrieval of both horizontal (east–west and north–south) and vertical displacement components. The combined use of different Sentinel-1 datasets enabled full spatial coverage of the rupture extent and a robust characterization of the seismogenic source, including its slip distribution. This comprehensive approach provides a solid analysis for subsequent investigations, including stress transfer modeling and assessment of the triggering potential of the nearby fault segments.

Abbreviations

SAR	Synthetic Aperture Radar
POT	Pixel Offset Tracking
MAI	Multiple Aperture Interferometry
InSAR	Interferometry Synthetic Aperture Radar
CFF	Coulomb Failure Function
IBR	Indo-Burman Ranges
MCB	Central Myanmar Basin
AFEAD	Active Faults of Eurasia Database
IWS	Interferometric Wide Swath
NCC	Normalized Cross-Correlation
DEM	Digital Elevation Model
ALOS	Advanced Land Observing Satellite
AZ	Azimuth
RG	Range
LoS	Line of Sight

Supplementary Information

The online version contains supplementary material available at https://doi.org/10.1186/s40645-026-00804-z.

Additional file1 (DOCX 2593 KB)

Acknowledgements
The authors want to thank Dr. Claudio Cesaroni for his support in the investigation of the ionospheric contribution in ALOS-2 data, the Japan Aerospace Exploration Agency (JAXA) for providing the ALOS-2 data, the European Space Agency (ESA) for their open data policy, and the Alaska Satellite Facility (ASF) for archiving Sentinel- 1 data.

Author contributions
VR, SP, SA, MM, and SS proposed the topic, conceived and designed the study. SP, SA, CT, AA, MP, PS, FM, MB, FC, CDL, and RL worked on the methodology and performed the analyses. All authors contributed to data interpretation and have read, reviewed, and approved the final manuscript.

Funding
Not applicable.

Data availability
The Interferometric Synthetic Aperture Radar (InSAR) data used in this article were collected by the Sentinel-1 satellites operated by the European Space Agency (ESA) and are freely available at the Alaska Satellite Facility (ASF, https://vertex.daac.asf.alaska.edu). ALOS-2 data were downloaded through the Japan Aerospace Exploration Agency (JAXA) GPortal (https://gportal.jaxa.jp/gpr/index/index). The Supplementary Material includes additional text, figures, and tables, providing more detailed insights into the methodology.

Declarations

Competing interests
The authors declare that they have no competing interests.

Received: 16 October 2025 Accepted: 8 February 2026
Published online: 04 March 2026

References

Atzori S, Hunstad I, Chini M, Salvi S, Tolomei C, Bignami C, Stramondo S, Trasatti E, Antonioli A, Boschi E (2009) Finite fault inversion of DInSAR coseismic displacement of the 2009 L'Aquila earthquake (central Italy). Geophys Res Lett. https://doi.org/10.1029/2009GL039293

Atzori S, Antonioli A (2011) Optimal fault resolution in geodetic inversion of coseismic data. Geophys J Int 185(1):529–538. https://doi.org/10.1111/j.1365-246X.2011.04955.x

Atzori S, Antonioli A, Tolomei C, De Novellis V, De Luca C, Monterroso F (2019) InSAR full-resolution analysis of the 2017–2018 M>6 earthquakes in Mexico. Remote Sens Environ 234:111461. https://doi.org/10.1016/j.rse.2019.111461

Bechor NBD, Zebker HA (2006) Measuring two-dimensional movements using a single InSAR pair. Geophys Res Lett. https://doi.org/10.1029/2006GL026883

Bradley K, Hubbard JA (2025) Updates on the M7.7 Myanmar earthquake. Earthquake Insights. https://doi.org/10.62481/9e49eb4a

Casu F, Manconi A, Pepe A, Lanari R (2011) Deformation time-series generation in areas characterized by large displacement dynamics: the SAR amplitude pixel-offset SBAS technique. IEEE Trans Geosci Remote Sens 49(7):2752–2763. https://doi.org/10.1109/TGRS.2010.2104325

Casu F, Manconi A, Pepe A, Manzo M, Lanari R (2010) Advances in the generation of deformation time series from SAR data sequences in areas affected by large dynamics. IEEE Int Geosci Remote Sens Symp 2010:2618–2621. https://doi.org/10.1109/IGARSS.2010.5651926

Costantini M (1998) A novel phase unwrapping method based on network programming. IEEE Trans Geosci Remote Sens 36(3):813–821. https://doi.org/10.1109/36.673674

Goldstein RM, Werner CL (1998) Radar interferogram filtering for geophysical applications. Geophys Res Lett 25(21):4035–4038. https://doi.org/10.1029/1998GL900033

Gray AL, Mattar, KE, Vachon PW, Bindschadler R, Jezek KC, Forster R, & Crawford JP (1998). InSAR results from the RADARSAT Antarctic Mapping Mission data: estimation of glacier motion using a simple registration procedure. In: IGARSS '98. Sensing and Managing the Environment. 1998 IEEE International Geoscience and Remote Sensing. Symposium Proceedings. (Cat. No.98CH36174), 3, 1638–1640 vol.3. https://doi.org/10.1109/IGARSS.1998.691662

Harris RA (1998) Introduction to special section: stress triggers, stress shadows, and implications for seismic hazard. J Geophys Res Solid Earth 103(B10):24347–24358. https://doi.org/10.1029/98JB01576

Hurukawa N, Maung Maung P (2011) Two seismic gaps on the Sagaing Fault, Myanmar, derived from relocation of historical earthquakes since 1918. Geophys Res Lett. https://doi.org/10.1029/2010GL046099

Jiang H, Feng G, Wang T, Bürgmann R (2017) Toward full exploitation of coherent and incoherent information in Sentinel-1 TOPS data for retrieving surface displacement: application to the 2016 Kumamoto (Japan) earthquake. Geophys Res Lett 44(4):1758–1767. https://doi.org/10.1002/2016gl072253

Marquardt DW (1963) An algorithm for least-squares estimation of nonlinear parameters. J Soc Ind Appl Math 11(2):431–441. https://doi.org/10.1137/0111030

Massonnet D, Feigl KL (1998) Radar interferometry and its application to changes in the Earth's surface. Rev Geophys 36(4):441–500. https://doi.org/10.1029/97RG03139

Massonnet D, Rossi M, Carmona C, Adragna F, Peltzer G, Feigl K, Rabaute T (1993) The displacement field of the Landers earthquake mapped by radar interferometry. Nature 364(6433):138–142. https://doi.org/10.1038/364138a0

Melgar D, Weldon R, Wang Y, Bato MG, Aung LT, Shi X, Wiwegwing W, Khaing SN, Min S, Thant M, Speed C, Zinke R, Fielding E, Meltzner A, Dawson T (2025) Supershear source model of the Myanmar earthquake and paleoseismology of the 2025 M7.8 sagaing Fault: regions of significant overlap with past earthquakes. Seismica. https://doi.org/10.26443/seismica.v4i2.1771

Menke W (1989) Geophysical data analysis: discrete inverse theory. Academic Press, San Diego

Mitchell A, Chung S-L, Oo T, Lin T-H, Hung C-H (2012) Zircon U–Pb ages in Myanmar: magmatic–metamorphic events and the closure of a neo-Tethys ocean? J Asian Earth Sci 56:1–23. https://doi.org/10.1016/j.jseaes.2012.04.019

Okada Y (1985) Surface deformation due to shear and tensile faults in a half-space. Bull Seismol Soc Am 75(4):1135–1154. https://doi.org/10.1785/BSSA0750041135

Petersen GM, Büyükakpinar P, Vera Sanhueza FO, Metz M, Cesca S, Akbayram K, Saul J, Dahm T (2023) The 2023 Southeast Türkiye seismic sequence: rupture of a complex fault network. Seismol Rec 3(2):134–143. https://doi.org/10.1785/0320230008

Scarr, S., Kawoosa, V. M., & Bankova, D. (2025). How a 'supershear' quake tore through Myanmar. Reuters. https://www.reuters.com/graphics/MYANMAR-QUAKE/SUPERSHEAR/zgvojlyojpd/ (last access: 22 September 2025)

Shahzada K, Noor UA, Xu Z-D (2025) In the wake of the March 28, 2025 Myanmar earthquake: a detailed examination. J Dyn Disasters 1(2):100017. https://doi.org/10.1016/j.jdd.2025.100017

Simpson RW, Reasemberg PA (1994) Earthquake-induced static stress changes on central California faults. US Geol Surv Prof Pap 1550-F:F55–F89

Socquet A, Vigny C, Chamot-Rooke N, Simons W, Rangin C, Ambrosius B (2006) India and Sunda plates motion and deformation along their boundary in Myanmar determined by GPS. J Geophys Res Solid Earth. https://doi.org/10.1029/2005JB003877

Stein RS, King GCP, Lin J (1992) Change in failure stress on the Southern San Andreas Fault System caused by the 1992 magnitude = 7.4 Landers earthquake. Science 258(5086):1328–1332. https://doi.org/10.1126/science.258.5086.1328

Takaku J, Tadono T, Doutsu M, Ohgushi F, & Kai H (2020). Updates of 'aw3d30' alos global digital surface model with other open access datasets. The International Archives of the Photogrammetry, Remote Sensing and Spatial Information Sciences, XLIII-B4-2020, 183–189. https://doi.org/10.5194/isprs-archives-XLIII-B4-2020-183-2020

Tin TZH, Nishimura T, Hashimoto M, Lindsey EO, Aung LT, Min SM, Thant M (2022) Present-day crustal deformation and slip rate along the southern sagaing fault in Myanmar by GNSS observation. J Asian Earth Sci 228:105125. https://doi.org/10.1016/j.jseaes.2022.105125

Thingbaijam KKS, Martin Mai P, Goda K (2017) New empirical earthquake source-scaling laws. Bull Seismol Soc Am 107(5):2225–2246. https://doi.org/10.1785/0120170017
USGSa. (2025). M 7.7 - 2025 Mandalay, Burma (Myanmar) Earthquake. https://earthquake.usgs.gov/earthquakes/eventpage/us7000pn9s/executive (last access: 22 September 2025)
USGSb. (2025). Search Earthquake Catalog. https://earthquake.usgs.gov/earthquakes/search/ (last access: 22 September 2025)
USGSc. (2025). M 6.7 - 2025 Burma (Myanmar) Earthquake. https://earthquake.usgs.gov/earthquakes/eventpage/us7000pn9z/moment-tensor (last access: 22 September 2025)
Vera F, Carrillo-Ponce A, Crosetto S, Kosari E, Metzger S, Motagh M, Liang Y, Lyu S, Petersen G, Saul J, Sudhaus H, Symmes-Lopetegui B, Than O, Xiao H, & Tilmann F (2025). Supershear Rupture Along the Sagaing Fault Superhighway: The 2025 Myanmar Earthquake. https://doi.org/10.22541/essoar.175034871.19414276/v1
Vigny C, Socquet A, Rangin C, Chamot-Rooke N, Pubellier M, Bouin M-N, Bertrand G, Becker M (2003) Present-day crustal deformation around Sagaing fault, Myanmar. J Geophys Res Solid Earth. https://doi.org/10.1029/2002JB001999
Walker KT, Shearer PM (2009) Illuminating the near-sonic rupture velocities of the intracontinental Kokoxili Mw 7.8 and Denali fault Mw 7.9 strike-slip earthquakes with global P wave back projection imaging. J Geophys Res Solid Earth. https://doi.org/10.1029/2008JB005738
Wang Y, Sieh K, Tun ST, Lai K-Y, Myint T (2014) Active tectonics and earthquake potential of the Myanmar region. J Geophys Res Solid Earth 119(4):3767–3822. https://doi.org/10.1002/2013JB010762
Wei S, Wang X, Li C, Zeng H, Ma Z, Shi Q, Chen H, Huang Y, Lyu M, Liao J, Yang S, Bai Y, Maung PM, Oo K, Htwe YMM, Zhang J, Zilio LD, Shan X, Chen L (2025) Supershear rupture sustained through a thick fault zone in the 2025 M w 7.8 Mandalay earthquake. Science 390(6772):468–475. https://doi.org/10.1126/science.adz2101
Williams CA, Wadge G (1998) The effects of topography on magma chamber deformation models: application to Mt. Etna and radar interferometry. Geophys Res Lett 25(10):1549–1552. https://doi.org/10.1029/98GL01136
Xu L, Meng L, Yunjun Z, Yang Y, Wang Y, Hu C, Weng H, Xu W, Su E, Ji C (2025) Bimaterial effect and favorable energy ratio enabled supershear rupture in the 2025 Mandalay earthquake. Science 390:476–481. https://doi.org/10.1126/science.ady6100
Zelenin E, Bachmanov D, Garipova S, Trifonov V, Kozhurin A (2022) The active faults of Eurasia database (AFEAD): the ontology and design behind the continental-scale dataset. Earth Syst Sci Data 14(10):4489–4503. https://doi.org/10.5194/essd-14-4489-2022
Zeng H, Ma Z, Li C, Yin X, Jiang Y, Chen Y, Rosakis A, Konca O, Wei S (2025) Super-shear and generalized Rayleigh rupture of the 2023 Turkey earthquake doublet influenced by fault material contrast. J Geophys Res Solid Earth. https://doi.org/10.1029/2025jb031560

Publisher's Note